Multi-MHz MEMS-VCSEL swept-source optical coherence tomography for endoscopic structural and angiographic imaging with miniaturized brushless motor probes

JASON ZHANG,[1,9] TAN NGUYEN,[1,9] BENJAMIN POTSAID,[1,2]
VIJAYSEKHAR JAYARAMAN,[3] CHRISTOPHER BURGNER,[3]
SIYU CHEN,[1] JINXI LI,[1] KAICHENG LIANG,[1] ALEX CABLE,[2]
GIOVANNI TRAVERSO,[4,5,6,7] HIROSHI MASHIMO,[7,8]
AND JAMES G. FUJIMOTO[1,*]

[1]*Department of Electrical Engineering and Computer Science, Research Laboratory of Electronics, Massachusetts Institute of Technology, Cambridge, MA 02139, USA*
[2]*Advanced Imaging Group, Thorlabs Inc., Newton, NJ 07860, USA*
[3]*Praevium Research Inc., Santa Barbara, CA 93111, USA*
[4]*Department of Mechanical Engineering, Massachusetts Institute of Technology, Cambridge, MA 02139, USA*
[5]*Division of Gastroenterology, Massachusetts General Hospital, Boston, MA 02114, USA*
[6]*Division of Gastroenterology, Brigham and Women's Hospital, Boston, MA 02115, USA*
[7]*Harvard Medical School, Boston, MA 02115, USA*
[8]*Veterans Affairs Boston Healthcare System, Boston, MA 02132, USA*
[9]*These authors contributed equally to this work*
[*]*jgfuji@mit.edu*

Abstract: Swept source optical coherence tomography (SS-OCT) enables volumetric imaging of subsurface structure. However, applications requiring wide fields of view (FOV), rapid imaging, and higher resolutions have been challenging because multi-MHz axial scan (A-scan) rates are needed. We describe a microelectromechanical systems vertical cavity surface-emitting laser (MEMS-VCSEL) SS-OCT technology for A-scan rates of 2.4 and 3.0 MHz. Sweep to sweep calibration and resampling are performed using dual channel acquisition of the OCT signal and a Mach Zehnder interferometer signal, overcoming inherent optical clock limitations and enabling higher performance. We demonstrate ultrahigh speed structural SS-OCT and OCT angiography (OCTA) imaging of the swine gastrointestinal tract using a suite of miniaturized brushless motor probes, including a 3.2 mm diameter micromotor OCT catheter, a 12 mm diameter tethered OCT capsule, and a 12 mm diameter widefield OCTA probe. MEMS-VCSELs promise to enable ultrahigh speed SS-OCT with a scalable, low cost, and manufacturable technology, suitable for a diverse range of imaging applications.

1. Introduction

Optical coherence tomography (OCT) enables micron scale, volumetric imaging of subsurface structures and pathology in biological tissues and materials [1]. SS-OCT uses wavelength swept lasers and high speed analog to digital conversion to achieve faster speeds and longer imaging ranges than spectral domain OCT [2]. Within the last decade, SS-OCT has achieved ultrahigh speeds, enabling applications such as widefield imaging of the eye [3], heartbeat intravascular OCT [4], OCT angiography (OCTA) [5], and optical coherence microscopy (OCM) [6]. Diverse medical applications of SS-OCT have been demonstrated in multiple specialties, including gastroenterology [7], dermatology [8], neurology [9], pulmonology [10], and gynecology [11].

SS-OCT has been used to assess pathology in situ and in real time [12], guide excisional biopsy [13], and assess surgical margins [14].

OCT has demonstrated potential to improve evaluation of gastrointestinal (GI) pathologies, including Barrett's esophagus and early esophageal adenocarcinoma [15,16]. However, comprehensive, widefield imaging is required to cover the large luminal area of the GI tract, and motion artifacts can potentially distort image features in the en face plane [17,18]. Ultrahigh speed A-scan rates can increase tissue coverage and reduce motion artifacts. However, speeds >2.0 MHz A-scan rate have not been demonstrated in the GI tract in vivo [19,20]. Moreover, operating parameters that balance tradeoffs between image coverage, motion artifacts, and sampling density at multi-MHz speeds in the GI tract have not been well investigated.

High speed, wavelength swept lasers have been essential to achieving ultrahigh A-scan rates [21]. Swept lasers include short cavity lasers [22], Fourier domain mode locked lasers (FDMLs) [23–26], dispersion tuned lasers [27,28], amplified spontaneous emission sweepers [29], stretched pulse lasers [30–36], and MEMS-VCSELs [37]. FDML lasers have been demonstrated at 5 MHz A-scan rates (20.8 MHz after 4X spot multiplexing) using 16X buffered sweeps [25], and commercial FDMLs are available up to 3.5 MHz with 8X buffered sweeps [38]. These lasers achieve high sweep rates, but are difficult to miniaturize and complex because kilometer-length fiber spools with optical amplifiers and active polarization control are required. Stretched pulse lasers operate at tens to hundreds of MHz A-scan rates and can image multi-centimeter fields of view. However, coherence lengths and imaging ranges are limited, and adjustable sweep rates are difficult to achieve because the rate is determined by the optical fiber length.

MEMS-VCSEL light source technology has compelling performance advantages for SS-OCT. It is a scalable, low cost, and manufacturable technology that achieves adjustable, multi-MHz A-scan rates without the need for sweep multiplexing. To our best knowledge, the MEMS-VCSEL is the only technology that can achieve high image acquisition speeds, long imaging range, and high resolutions with operating parameters that can be varied over orders of magnitude within a single device. The sweep rate and range can be varied to support different A-scan rates, resolution, and imaging ranges with a given analog to digital converter (ADC) digitization rate [3]. The small mirror mass and adiabatic tuning of the MEMS-VCSEL enable multi-MHz sweep rates over a broad range >100 nm [39].

In this paper, we describe MEMS-VCSEL SS-OCT technology at A-scan rates of 2.4 and 3.0 MHz. Sweep to sweep calibration and resampling are performed using dual channel acquisition of the OCT signal and a Mach Zehnder interferometer signal, overcoming inherent optical clock limitations and enabling higher performance. We demonstrated structural and angiographic imaging in swine using a 3.2 mm diameter micromotor OCT catheter, a 12 mm diameter tethered OCT capsule, and a 12 mm diameter widefield OCTA probe. We describe representative applications, including high resolution structural and angiographic imaging, widefield volumetric mapping, and widefield OCTA, describing parameter selection for each application. Although this manuscript focuses on gastrointestinal imaging, MEMS-VCSEL SS-OCT technology can also be used for many other applications, including laparoscopic and minimally invasive imaging as well as non-destructive evaluation and testing.

2. Experimental setup and methods

2.1. OCT system overview

Figure 1 shows a schematic of the SS-OCT instrument, which used a multi-MHz MEMS-VCSEL and dual channel, sweep to sweep calibration with a 2 gigasamples-per-second (GSPS) ADC board (ATS9373, Alazar Inc.). Many prior ultrahigh speed SS-OCT systems used an optical *k*-clock in order to sample OCT fringes linearly in wavenumber. However, this method did not operate reliably above 1.3 GSPS and was susceptible to clocking glitches and sampling errors [40,41], making multi-MHz speeds challenging. The dual channel approach of this paper

acquires both OCT and MZI fringes for every A-scan at the full ADC digitization rate (2 GSPS) to achieve improved OCT data quality, but at a cost of additional computation.
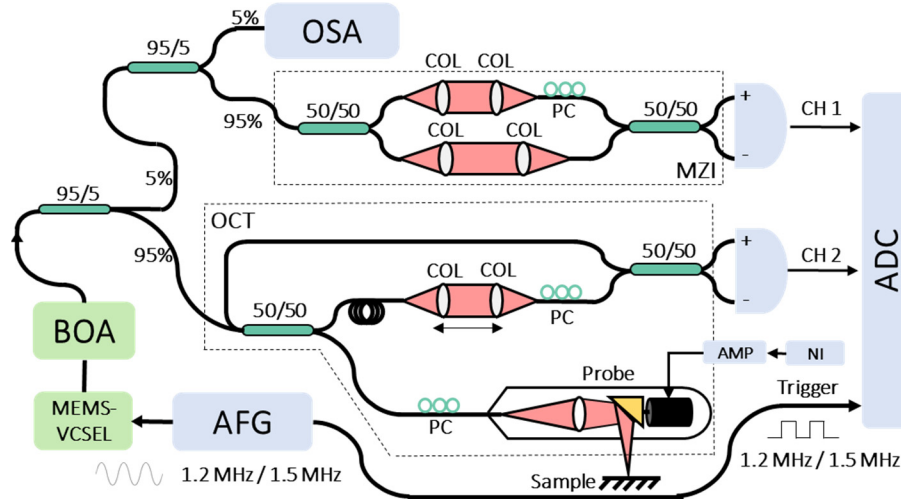

Fig. 1. Schematic of the SS-OCT system. Sweep to sweep calibration and resampling are performed using dual channel acquisition of the OCT signal and a Mach Zehnder interferometer signal, overcoming inherent optical clock limitations and enabling higher performance. ADC: analog to digital converter, AFG: arbitrary function generator, AMP: 3-phase linear amplifier, BOA: booster optical amplifier, COL: collimator, PC: polarization controller, NI: National Instruments card, OSA: optical spectrum analyzer.

Other ultrahigh speed SS-OCT systems used a single channel approach in which a single representative MZI calibration trace was used to calibrate all the A-scans in the data set. If the laser sweep is stable, an MZI calibration fringe from a single sweep can be used to resample OCT signal fringes from different sweeps, resulting in a significant reduction in computational load. However, MEMS-VCSELs can have sweep to sweep variations in the wavenumber (frequency) versus time, which will cause errors in distance measurement and fluctuations in the axial point spread function (PSF). To calibrate for this sweep variation, we acquire every OCT fringe simultaneously with an MZI fringe and compute a sample (time) to wavenumber (frequency) calibration for each A-scan.

The MEMS-VCSEL used a new design with higher MEMS actuator stiffness to increase the mechanical resonance to >1 MHz, compared to 300-400 kHz in previous publications [37]. The MEMS was driven by sinusoidal voltage waveforms at 1.2 or 1.5 MHz using an arbitrary function generator (AFG) (AFG3102, Tektronix, Inc.) and high voltage amplifier (Model 2100HF, Trek, Inc.). Fringes from both the up and down sweeps were sampled, resulting in effective A-scan rates of 2.4 MHz or 3.0 MHz. Other A-scan rates could be obtained by using different MEMS drive waveforms. The VCSEL wavelength sweep range was 113 nm (1235-1348 nm) at 2.4 MHz and 106 nm (1242-1348 nm) at 3.0 MHz, measured by an optical spectrum analyzer (OSA) (Fig. 2). The VCSEL output was amplified using a prototype high power booster optical amplifier (BOA) (Thorlabs, Inc.) to achieve ~130 mW of average power.

The OCT interferometer had a transmission mode reference arm to account for variations in sample arm path differences of different imaging devices. Circulators were not used in order to avoid polarization mode dispersion [42,43]; as a result, this reduced the overall power delivery and signal collection efficiency. The MZI was adjusted to generate a maximum fringe frequency of ~430 MHz at 2.4 MHz and ~530 MHz at 3.0 MHz, which were sufficiently high to provide an
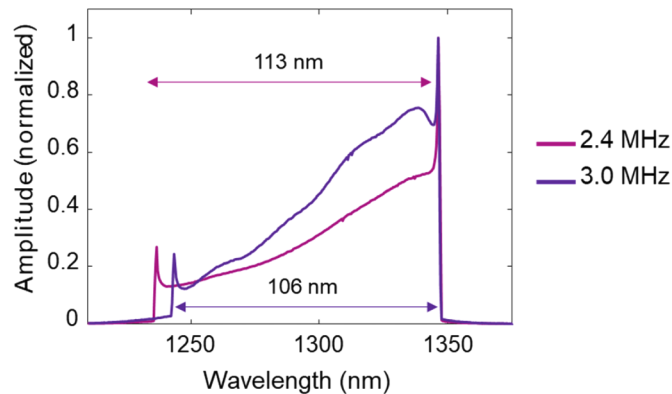
Fig. 2. Wavelength sweep range of the MEMS-VCSEL measured with an integrating optical spectrum analyzer at 2.4 MHz and 3.0 MHz A-scan rate.

accurate wavenumber (frequency) versus sample (time) measurement of the sweep. Polarization controllers were used to align the sample and reference arm polarizations, maximizing fringe visibility across the sweep.

OCT and MZI signals were detected by InGaAs balanced photodetectors with a 1.6 GHz radiofrequency (RF) bandwidth (PDB480C-AC, Thorlabs, Inc.). The fringes were digitized by a high-speed 12-bit ADC (ATS9373, Alazar Technologies, Inc.) in a workstation computer (Windows 10 Pro x64, 64 GB RAM, Intel Xeon CPU-ES-1650v3, NVIDIA RTX2080Ti GPU). The acquisition was synchronized by a trigger signal from the AFG. An auxiliary I/O channel from the ADC was used to synchronize data acquisition with the motor drive signal from a multifunction card (NI-6323, National Instruments, Inc.). A custom multi-threaded C++ program using GPU processing (CUDA Toolkit 10.0, Nvidia) controlled data acquisition, motor actuation, hardware synchronization, OCT and MZI signal processing, and real-time display.

2.2. Imaging probes

We used three different devices to demonstrate complementary OCT and OCTA imaging applications (Fig. 3). The micromotor OCT catheter (Fig. 3(A)) had a 3.2 mm outer diameter (OD) and a 20 μm full-width-at-half-maximum (FWHM) transverse optical resolution.

The catheter has been described in a previous publication [44] and can be introduced through an endoscope accessory port for positioning under endoscopic guidance. A reflective microprism on a 2 mm diameter, brushless, sleeve bearing DC micromotor (DBL02-06H1, Namiki Precision) was used to circumferentially scan the OCT beam from a fiber GRIN focuser. The optics and micromotor were in a brass housing and attached to a torque coil in a transparent fluorinated ethylene propylene (FEP) sheath (AWG9, Zeus, Inc.). Volumetric OCT datasets were acquired by rapidly scanning the beam circumferentially and longitudinally retracting (pulling back) the torque coil and optics assembly with a proximal translation stage (LP28, Parker Hannifin Motion and Control, Inc.) to generate a dense helical scan. The brass housing obscured ~40% of the circumference, resulting in a ~6 mm effective circumferential FOV.

We also demonstrated imaging with a tethered OCT capsule designed for widefield volumetric OCT mapping of long luminal structures, such as the esophagus. The tethered OCT capsule was 12 mm in diameter and 28 mm long, similar to that described in a previous publication [45]. The transverse optical resolution was 30 μm FWHM. The current capsule used custom-machined ultrahigh molecular weight (UHMW, Bodeker Plastics) plastic distal and proximal caps joined by a ~1 mm thick, 12 mm diameter glass imaging window (Fig. 3(B)). UHMW plastic improved the lubricity for smoother pullback, reducing image distortion caused by non-uniform longitudinal
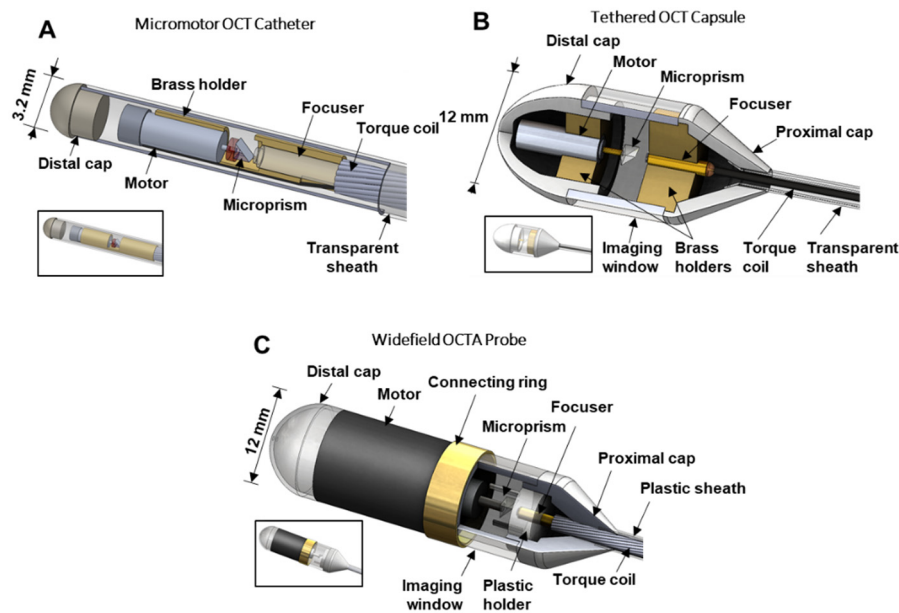
Fig. 3. 3D models of the imaging probes used in this study, including the (A) micromotor OCT catheter (B) tethered OCT capsule, and (C) widefield OCTA probe.

motion. A microprism and 3 mm diameter, brushless, ring jewel bearing DC motor (0308H003B, Faulhaber Micromo, LLC) circumferentially scanned the OCT beam from a fiber GRIN focuser. A semi-rigid tether was used to manually advance the capsule to regions of interest and then retract it (pulled back) to acquire volumetric data.

Finally, we demonstrated a widefield probe for OCT and OCTA of large diameter, shallow luminal or cavity structures. OCTA visualizes blood flow using differences between repeated OCT images and is especially challenging because it requires stable circumferential beam scanning, as well as slow, constant speed longitudinal actuation. The probe was 12 mm in diameter and 47 mm long and was attached to a semi-rigid tether for longitudinal actuation (Fig. 3(C)). The transverse optical resolution was 30 µm FWHM. Prior studies showed that the sleeve bearing DC micromotor and brushless DC motor used in the first two probes had insufficient rotational uniformity for OCTA. Therefore, a 12 mm diameter, brushless, ball bearing DC motor (1226S006B, Faulhaber Micromo, LLC) was used to achieve the high rotational stability required for OCTA imaging. The distal and proximal caps and motor were covered with polytetrafluoroethylene (PTFE) heat shrink tubing to improve lubricity (not shown), and the polystyrene (PS) imaging window was joined with the motor using a connecting ring. The semi-rigid tether was used to facilitate manual introduction and retraction of the probe. This probe could image shallow luminal structures, where the tether length could be short enough to provide the uniform speed pullback required for OCTA imaging. Table 1 summarizes the different probe constructions.

2.3. Motor stability for OCTA

Circumferentially scanning OCT probes must perform a uniform rotational scan to obtain high-quality OCT and OCTA data. Fluctuations in angular position vs. time will cause the positions of the A-scans on the tissue to vary. The scan stability is important for wide FOV imaging because the circumferential spacing between A-scans versus angular position will scale with the probe radius. Scan stability is especially important in OCTA because blood flow is visualized by detecting changes between repeated OCT scans over the same location. Fluctuations

Table 1. Imaging Probe Specifications

Probe Type	Diameter [mm]	Resolution FWHM [μm]	Motor Dimensions (dia. × length) [mm]	Bearing Type	Rotation Rate (RPM)	Window Material	Window Thickness [mm]
Micromotor OCT Probe	3.2	20	2 × 6	Sleeve	36,000-90,000	FEP	0.2
Tethered OCT Capsule	12	30	3 × 8	Ring jewel	66,000	Glass	1
Widefield OCTA Probe	12	30	12 × 26	Ball bearing	36,000	PS	1

in the scanning will cause background differences or decorrelations that can obscure vasculature. We measured the rotational uniformity of the three motors to assess scan stability. A laser diode beam was reflected into a photodiode from a microprism attached to the motor shaft. Each motor rotation generated a transient photodiode signal which was detected by an oscilloscope and the time between peaks T was used to measure the rotational period.

2.4. Signal processing

OCT and MZI interference fringes were digitized at 2 GSPS (12 bits ADC) with 1280 and 1024 samples per sweep at 2.4 MHz and 3.0 MHz A-scan rates, respectively. Fringe signals were upsampled by 4x to 5120 and 4096 samples and multiplied by a phase vector to correct for the detector nonlinear phase response. The method for obtaining this phase correction vector, as well as numerical dispersion correction coefficients and group velocity time delay, has been previously published [46].

To perform sweep to sweep wavenumber calibration, we calculated the instantaneous phase of the MZI fringe. The fringes were parsed into up and down sweeps and the down sweep was time reversed. The fringes were Hilbert transformed and phase unwrapped to determine the phase at each sample. If the MZI is stable, the starting phase of each sweep is known up to a 2π ambiguity, enabling each sweep to be registered at a reference value. The up and down sweeps were phase registered by adding an integer multiple of 2π to the sweep phase, so the phase at the reference sample was shifted to be within $[-\pi, \pi]$ radians. The reference sample was chosen close to the sweep turn-around point. Then, all sweeps within a B-scan were registered to each other so the phase difference at all reference sample points was between $[-\pi, \pi]$. This ensured that all sweeps in the B-scan covered approximately the same phase and wavelength range.

Next, using the estimated phase, we resampled the OCT fringes to be linear in wavenumber using spline interpolation. Numerical dispersion compensation was applied to the resampled fringes before Fourier transformation. The B-scans were registered using a non-uniform rotational distortion (NURD) correction algorithm [41] and log-compressed for display. En face images were generated by averaging OCT signal over the full axial depth and displayed using a square root scale.

OCTA was calculated using amplitude decorrelation of two adjacent linear OCT signal B-scans using the formula [47]

$$D_n(x, z) = \frac{[A_n(x, z) - A_{n+1}(x, z)]^2}{A_n^2(x, z) + A_{n+1}^2(x, z)} = 1 - \frac{A_n(x, z)A_{n+1}(x, z)}{0.5A_n^2(x, z) + 0.5A_{n+1}^2(x, z)}, \tag{1}$$

where $D_n(x,z)$ is the nth amplitude decorrelation frame as a function of spatial pixel coordinates x and z in the fast scan direction and depth, respectively, and $A_n(x,z)$ is the nth NURD corrected B-scan in linear scale. Amplitude decorrelation is calculated at each pixel (x,z). To reduce

decorrelation noise from tissue or probe motion, we used a two step algorithm. The first step applied a mask generated from B-scans that were averaged $(A_n+A_{n+1})/2$ and Gaussian filtered ($\sigma = 0.5$ pixels) to D_n. This mask was computed by identifying all pixels with an average amplitude above a threshold, selected to be about three times the noise deviation in a region without tissue. The second step rejected pixels in D_n with a small decorrelation amplitude. The thresholding value was manually selected for each dataset to optimize the vessel visibility. Smaller thresholds retained smaller vessels at the cost of greater noise, while larger thresholds rejected more noise but reduced visibility of smaller vessels. Our implementation used a smaller OCTA threshold with a noisier background to improve the visibility of smaller vessels. To reduce noise, we applied median filtering along the longitudinal pullback dimension with a filter length of 5 B-scans, assuming the OCTA signal from a true blood vessel was likely to persist longer than background noise. En face OCTA images were generated using either the mean of OCTA signal over 10 μm axial depth or over the full axial depth, depending on whether visualization of depth resolved vasculature was needed.

2.5. Swine imaging procedure

The multi-MHz SS-OCT system and imaging probes were tested in swine because their GI tracts are similar to that of humans. Five adult Yorkshire swine were imaged under a protocol approved by the MIT Committee on Animal Care. The swine were restricted from food and water 8-12 hours before anesthesia, and a pre-medication of 0.04 mg/kg intramuscular atropine was used to avoid vagal reflexes, control respiration, and control salivation. Veterinary staff anesthetized swine with intramuscular 5 mg/kg telazol and 2 mg/kg xylazine. Temperature, heart rate, and respiratory rate were monitored throughout the procedure. After being placed in a supine or lateral decubitus position, the swine was covered with a heating blanket, and bite blocks were placed. Before rectal imaging, an enema was performed to clear the rectum of stool.

The micromotor OCT catheter was used for esophageal and rectal imaging. In the esophagus, the probe was introduced through the endoscope accessory port and positioned against the region of interest. In the rectum, the catheter was directly introduced without the endoscope. The torque cable and optics were proximally retracted through the stationary catheter sheath by a motorized translation stage to acquire volumetric data. The tethered OCT capsule was introduced using an overtube for widefield volumetric mapping of the upper GI tract. The capsule was advanced and then longitudinally retracted to acquire volumetric data. Distance markings on the tether were used to estimate the longitudinal pullback distance by visual inspection. The widefield OCTA probe was manually introduced and retracted for imaging the anorectal region. The shallow insertion depth in the lower GI tract provided a more uniform longitudinal actuation than in the upper GI tract, enabling OCTA.

2.6. Scan protocols

Table 2 summarizes the different scan protocols used to demonstrate endoscopic imaging applications. The 3.2 mm micromotor OCT catheter was evaluated for high resolution structural and angiographic imaging of the esophagus and rectum. For high resolution structural imaging, we used a fast rotational (B-scan) rate with fast pullback speed to maximize sampling density and coverage. For esophageal imaging, a 3.0 MHz A-scan rate was used and the micromotor was operated at 1500 Hz (B-scans per second) with an 18 mm/sec pullback speed for 2.3 seconds (12 μm spacing between B-scans). For rectal imaging, a 2.4 MHz A-scan rate was used and the micromotor was operated at 1000 Hz (B-scans per second) with a 4 mm/sec pullback speed for 7 seconds (4 μm B-scan spacing). The pullback speed for esophageal imaging was ~4x faster than for rectal imaging to reduce breathing, heartbeat, and peristaltic wave artifacts. For OCTA imaging, denser sampling in both the circumferential and longitudinal dimension was necessary. Therefore, the micromotor was operated at 600 Hz and a slower pullback speed of 2 mm/sec for

9 seconds were used (3 μm B-scan spacing). This sets a limit on the slowest blood flow speeds (smallest vessels) that can be detected.

Table 2. Scan Protocol Parameters

Probe Type	Application	FOV (mm)	A-scan Rate (MHz)	B-scan Rate (Hz)	A-scans / B-scan	Pullback Speed (mm/s)	B-scan Spacing (μm)
Micromotor OCT Catheter	Esophagus OCT	6	3.0	1500	2000	18	12
Micromotor OCT Catheter	Rectal OCT	6	2.4	1000	2400	4	4
Micromotor OCT Catheter	Esophagus OCTA	6	2.4	600	4000	2	3
Tethered OCT Capsule	Esophagus OCT	38	3.0	1100	2727	30	27
Widefield OCTA Probe	Anorectal OCT/OCTA	38	2.4	600	4000	3	5

The tethered OCT capsule was used to demonstrate rapid, wide FOV imaging of the esophagus. A 3.0 MHz A-scan rate was used and the 3 mm motor was operated at 1100 Hz (B-scan rate) with a ~30 mm/sec pullback speed for 5 seconds. This enabled imaging of a ~40 mm x 150 mm region of the esophagus with a B-scan spacing of 27 μm. This pullback speed was fast enough to minimize jumping/sticking during the acquisition while maintaining sufficient sampling in the longitudinal dimension to visualize en face structural features.

The widefield OCTA probe was used to demonstrate wide FOV OCT/OCTA of the anorectal region. A 2.4 MHz A-scan rate was used, and the 12 mm motor was operated at 600 Hz (B-scan rate) with a ~3 mm/sec pullback speed for 7 seconds. OCTA requires repeating scanning of the same region, so a slower motor speed was used compared with the tethered OCT capsule. The B-scan spacing was 5 μm, similar to the micromotor OCTA of the esophagus, except the widefield OCTA probe B-scans covered a ~40 mm circumferential FOV compared to the ~6 mm FOV of the micromotor probe.

The widefield OCTA probe was proximally pulled back using a short tether to achieve a uniform longitudinal speed. The slower pullback speeds increase repeated B-scan overlap, which improves OCTA image quality. The tethered OCT capsule could not be used for OCTA because the motor was not stable enough and pullback using the longer tether had longitudinal speed fluctuations, which generated OCTA artifacts.

3. Results

3.1. System performance

System sensitivity and sensitivity roll off were measured using a mirror in the sample arm and a 40 dB (double pass) attenuation. The reference arm power was set to ~1 mW, optimizing heterodyne gain while limiting excess noise. Sensitivity roll off versus range was measured at 100 μm increments.

At 2.4 MHz A-scan rate and 20 mW incident power, the sensitivity was 101 dB. The axial resolution measured from the PSF was 16.0 μm FWHM in air (~12.3 μm in tissue), and side lobes were minimized using a Taylor window (24 equiripple sidelobes, −30 dB sidelobe suppression) (Fig. 4(A)). The FWHM was slightly larger than our previous results (13.5 μm in air from Ref. [6]) because the VCSEL spectrum was asymmetric (Fig. 2) in contrast to the flatter spectrum in [6], and the BOA gain-bandwidth was slightly mismatched to the VCSEL sweep range. Point spread functions and image range were measured using attenuated reflections from a mirror at different distances set by a translation stage (Fig. 4(B)). Since the MEMS-VCSEL wavelength

sweep is approximately sinusoidal in time, the highest OCT fringe frequencies occur at the center of the sweep. The image range was defined as the distance where the highest frequency fringe signal will begin to exceed the 1 GHz Nyquist limit of the 2 GSPS ADC. At 2.4 MHz A-scan rate, the image range is ~1.8 mm in air. At larger delays, the maximum OCT fringe frequency will begin to alias, causing broadening of the point spread function, increased sidelobes and sensitivity roll off. At delays less than 1.8 mm, sensitivity is nearly constant with depth.
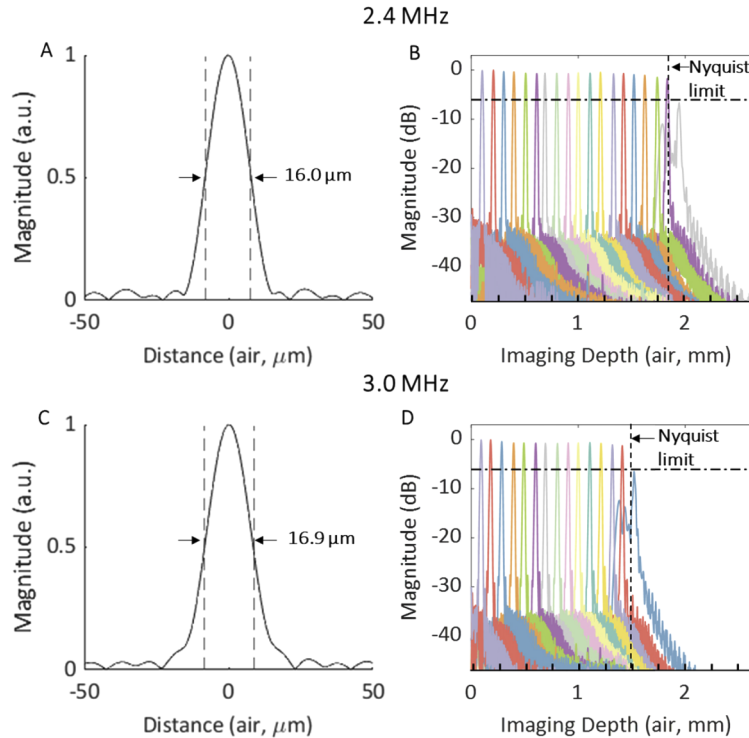
Fig. 4. (A) Point spread function for 2.4 MHz A-scan rate, shown in linear scale. (B) Corresponding sensitivity roll off in logarithmic scale. Dot-dashed line is −6 dB below the maximum PSF value. Dashed line shows the maximum depth/fringe frequencies (prior to wavenumber calibration) corresponding to the ADC 1 GHz Nyquist limit. (C) Point spread function for 3.0 MHz A-scan rate, shown in linear scale. (D) Corresponding sensitivity roll off in logarithmic scale.

At 3.0 MHz A-scan rate and 20 mW incident power, the sensitivity was 100 dB. The axial resolution was 16.9 μm FWHM in air (~13.0 μm in tissue), and side lobes were reduced using a Taylor window (8 equiripple sidelobes, −35 dB sidelobe suppression) (Fig. 4(C)). The slightly larger axial resolution compared to 2.4 MHz operation is likely due to the reduced sweep range. The 3.0 MHz A-scan rate has higher fringe frequencies than 2.4 MHz operation and the image range was reduced to ~1.5 mm in air (Fig. 4(D)). The narrow instantaneous linewidth of the VCSEL can support much longer ranges if ADC sampling rates are increased.

3.2. Motor stability

The selection of micromotors for the different probes was based on measurements of motor stability. To quantify stability, we measured the period T_n for the nth rotation, which varies if the rotation is unstable. Variations in period $\delta T_n = T_n - T_{n-1}$ indicate variations in the circumferential scan velocity, which change the number of A-scans per rotation. Normalizing δT_n with the period

T_n gives the fractional change in period, which is a dimensionless quantity that characterizes the motor stability independent of the rotation speed. Multiplying this dimensionless quantity with the probe circumference C gives a quantity $\delta S_n = C \times \delta T_n / T_n$ that describes a differential displacement along the probe circumference (units of length).

Plots of $\delta T_n / T_n$ and δS_n for the three motors are shown (Fig. 5). The 12 mm diameter ball bearing motor had the most uniform scanning, with $\delta T_n / T_n$ between -3×10^{-4} and 2×10^{-4} (Fig. 5(A)) and was used for the widefield OCTA probe. The 3 mm diameter ring jewel bearing motor (Fig. 5(B)) used for the tethered OCT capsule and the 2 mm diameter sleeve bearing motor used for the micromotor OCT catheter (Fig. 5(C)) had worse scanning performance with larger $\delta T_n / T_n$ relative to the 12 mm ball bearing motor. Similarly, the 12 mm ball bearing motor had a smaller δS_n amplitude compared to the other two motors. Although the ring jewel bearing motor is more stable than the sleeve bearing motor, the δS_n of the two are comparable because the circumference of the 12 mm diameter tethered OCT capsule is larger than the circumference of the 3.2 mm diameter catheter. Larger diameter probes which image wider fields of view require higher stability scanning. The standard deviation (SD) of δS_n, $\sigma_{\delta S}$, for the 12 mm ball bearing motor (3.18 μm) was 13X smaller than that of the 3 mm ring jewel motor (40.3 μm) and 19X smaller than that of the 2 mm sleeve bearing motor (60.7 μm) (Fig. 6). A similar trend is seen with the mean of the absolute value of δS_n, $<|\delta S_n|>$ (Fig. 6). The improved scan stability may
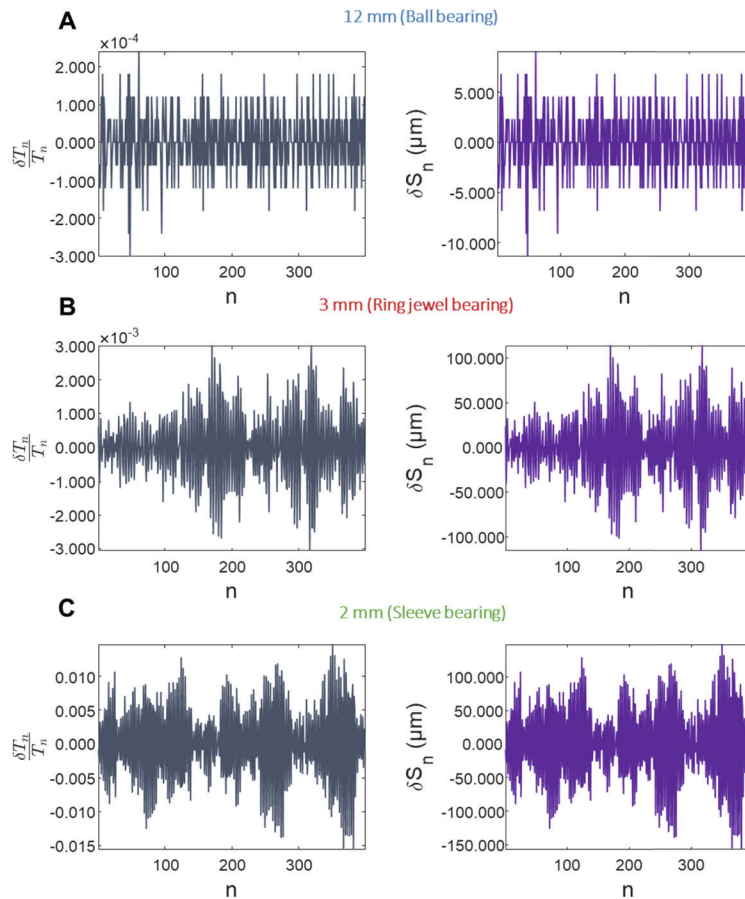

Fig. 5. Fractional rotational period variation $\delta T_n / T_n$ and position variation δS_n versus rotation n (time) for the sleeve, jewel, and ball bearing motors.

also be due to the larger rotational inertia of the ball bearing motor (0.15 g·cm^2), which smooths the rotation. The rotational inertias of the 3 mm ring jewel bearing motor and 2 mm sleeve bearing motor were $2·10^{-4}$ g·cm^2 and $4.3·10^{-5}$ g·cm^2, respectively.
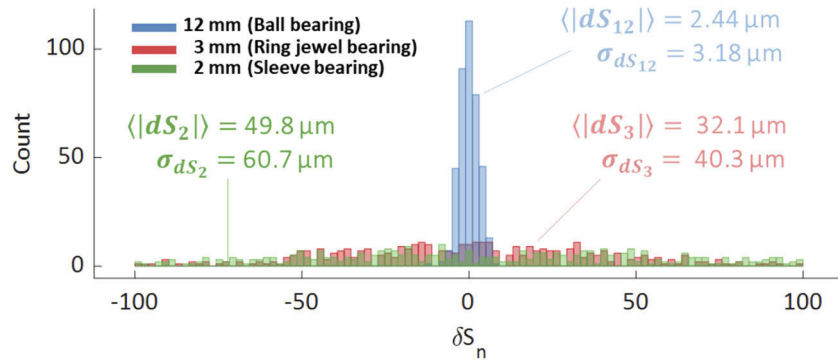

Fig. 6. Histogram of δS_n, the differential displacement along the probe circumference, and standard deviations in μm for the three motor types. The mean of the absolute value $<|\delta S_n|>$ is also shown.

3.3. High resolution OCT structural imaging

High resolution structural imaging was demonstrated in swine esophagus and rectum using the micromotor OCT catheter, which had high spatial resolution and a fast B-scan rate for dense longitudinal sampling. The micromotor catheter had a ~6 mm circumferential FOV, limited by the struts of the motor mount, and imaging was performed over a 30-40 mm longitudinal pullback. Figure 7(A-(C)) shows esophageal images acquired by positioning the catheter using both endoscopic visualization and real-time B-scan display. The pullback speed was 18 mm/sec, corresponding to a 12 μm B-scan spacing and a ~40 mm long region was imaged. This pullback speed was chosen to reduce artifacts from peristaltic, cardiac, and respiratory motion. The en face image spanned a region of squamous epithelium (Fig. 7(A)), which had a smoother appearance compared to columnar epithelium. The enlarged en face image shows a large, hypo-scattering vessel (Fig. 7(B)). The cross sectional image also shows the characteristic layered architecture of esophageal mucosa and submucosa: the squamous epithelium, lamina propria, muscularis mucosa, and submucosa (Fig. 7(C)).

Figures 7(D-(F)) show rectal images acquired by positioning the catheter against a region of interest using the real-time B-scan display. The pullback speed was ~4 mm/sec, corresponding to a 4 μm B-scan spacing, and a ~30 mm long region was imaged. The relatively slow pullback and fine B-scan spacing enabled visualization of microscopic features of normal rectal tissue. The en face image showed good contact over the 30 mm pullback (Fig. 7(D)) and visualized columnar crypt structures appearing as regular, ovular features (Fig. 7(E)). In the cross sectional image, highly scattering columnar crypts appeared as bright vertical features interspersed with darker regions of lamina propria and cast axial projection artifacts to deeper depths (Fig. 7(F)). These are characteristic microarchitectural features of normal columnar epithelium [48].

In the esophagus, the probe partially lost contact with the mucosa for ~1/3rd of the pullback, but signal was strong in regions of contact. The faster B-scan rates and pullback speeds reduced artifacts in the en face image caused by non-uniform longitudinal pullback. Some degree of longitudinal distortion occurred due to friction between the torque cable and sheath, especially when the catheter was sharply bent. However, longitudinal motion distortion due to non-uniform longitudinal pullback was much lower than in manually actuated capsules or probes.
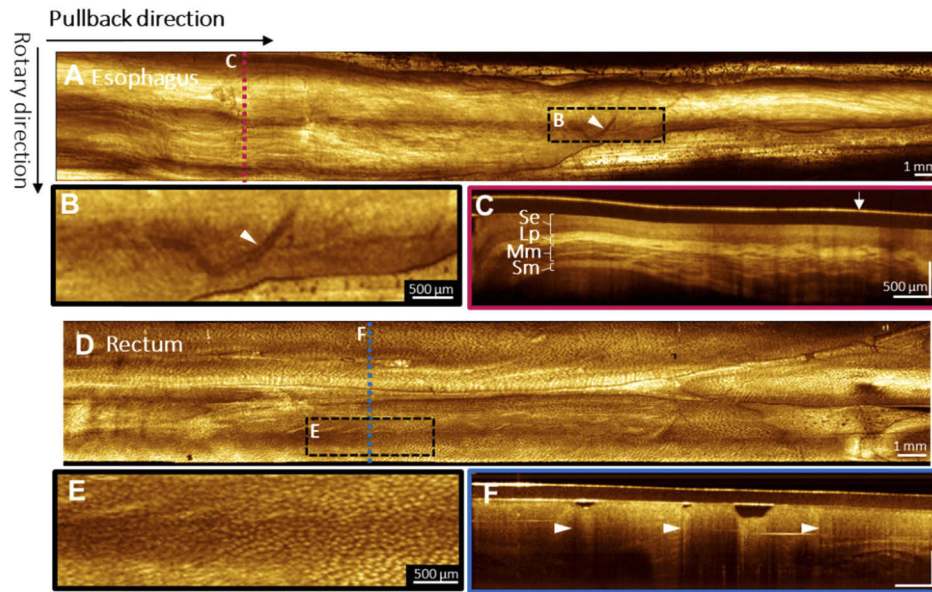
Fig. 7. (A) Micromotor OCT catheter structural imaging of the esophagus, covering a 40 mm pullback distance. Pullback is performed rapidly to reduce physiological motion artifacts. Arrowheads denote a large vessel visible as a hypo-scattering contour in the (B) enlarged en face image. (C) Cross sectional image shows the layered appearance of esophageal mucosa and submucosa. Arrow points to a reflection from the catheter sheath. (D) High resolution micromotor OCT catheter structural imaging of swine rectum, covering a longitudinal pullback distance of 30 mm. (E) The enlarged en face region shows columnar epithelial crypts appearing as regular, ovular features. (F) The cross sectional image shows characteristic, highly-scattering vertical projection features from columnar epithelium, marked by arrowheads. Se: squamous epithelium, Lp: lamina propria, Mm: muscularis mucosa, Sm: submucosa.

3.4. High resolution OCT angiography imaging

High resolution OCTA imaging using the micromotor OCT catheter was demonstrated in the swine esophagus. The B-scan rate was 600 Hz and a slow pullback speed of 2 mm/sec was used to acquire partially overlapping B-scans. The time between B-scans (interscan time) was ∼1.6 ms, and the B-scan spacing was 3 µm. Figure 8 shows representative OCT images and corresponding depth resolved en face OCTA images. The cross sectional image shows the layered appearance of esophageal mucosa and submucosa (Fig. 8(B)).

Although larger vessels were visible in the structural en face OCT image as hypo-scattering contours, OCTA visualizes a more elaborate branching vascular structure (Fig. 8(C-(F))). Enlarged regions of the en face OCTA image show vessel structure at different axial depths (Fig. 8(G-(J))). Smaller vessels are visible in more superficial layers, ∼300 µm below the tissue surface (Fig. 8(G)), while larger vessels are visible in the lamina propria and submucosa, >650 µm below the surface (Fig. 8(H-(J))), consistent with the morphology of normal esophagus. OCTA decorrelation signals from non-uniform longitudinal motion or rotational scan variation generate vertical stripes in the en face image.

3.5. Widefield volumetric mapping

Widefield volumetric mapping of the swine upper GI tract was demonstrated using the tethered OCT capsule (Fig. 9). The tethered capsule enabled imaging a ∼5,700 mm² region in 5 seconds
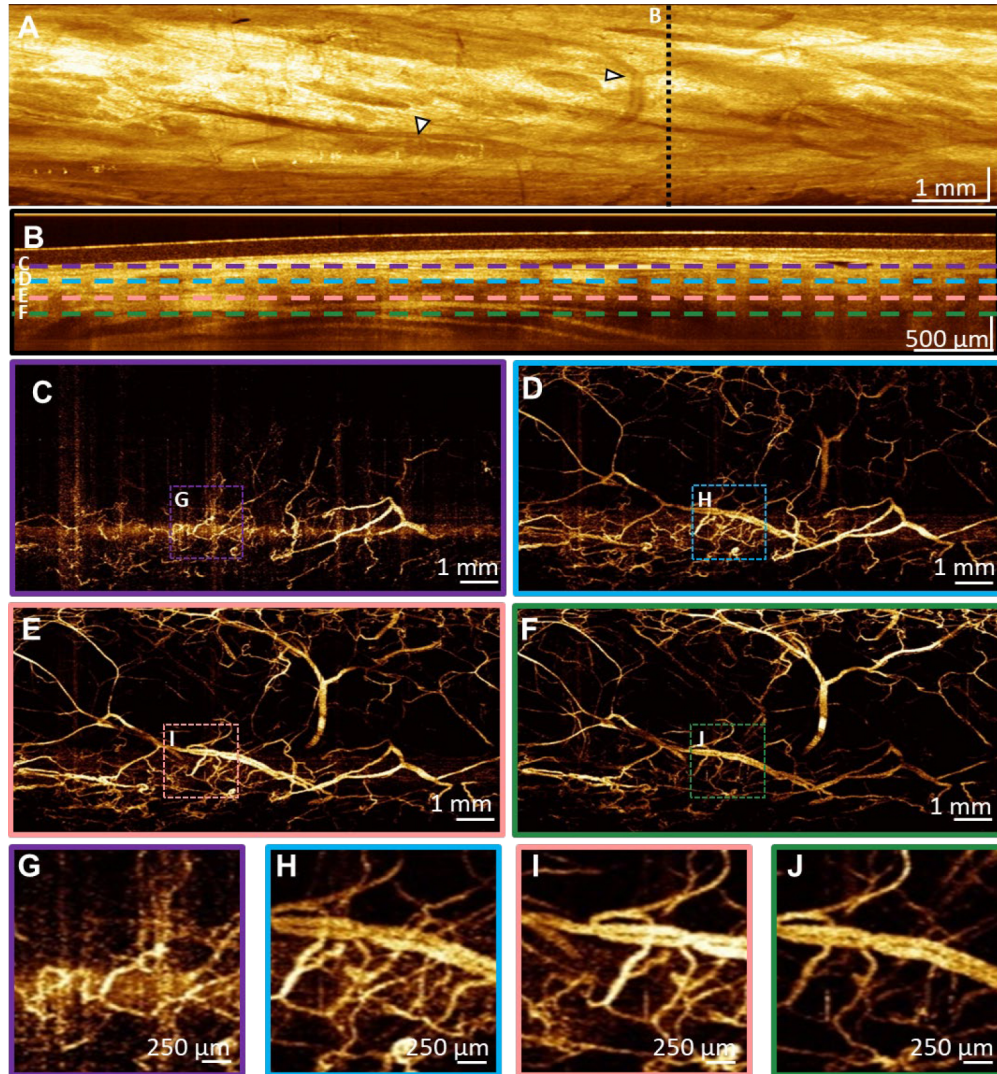
Fig. 8. (A) Micromotor probe OCT of the swine esophagus, covering a 14 mm longitudinal pullback distance. En face OCT image shows vessels (arrowheads) and esophageal mucosa with its characteristic smooth appearance. (B) Cross sectional image shows subsurface layered appearance of esophageal mucosa. (C-F) En face OCTA projections over 10 μm at four different depths (300 μm, 650 μm, 1 mm, and 1.35 mm below the surface) show depth resolved vasculature not visible in the structural en face image. (G-J) Enlarged en face OCTA images showing elaborate branching vasculature and appearance of larger vessels at deeper depths.

visualizing distinct anatomical and microarchitectural landmarks in a single pullback. Figure 9 shows a representative volumetric data set. The widefield enabled zooming and panning in the en face plane to visualize esophageal and gastric tissue at different spatial scales. The en face image of the full FOV shows the gastroesophageal junction (GEJ) delineating gastric and esophageal tissue (Fig. 9(A)).
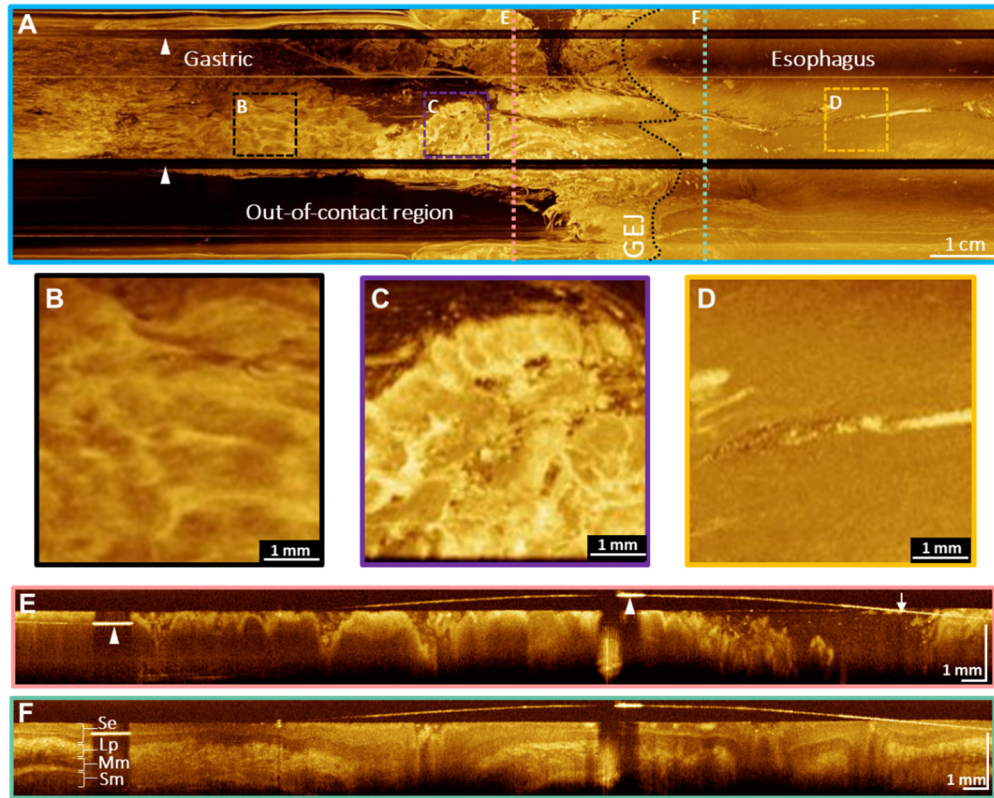

Fig. 9. (A) Tethered OCT capsule imaging of the swine upper GI tract, covering a 150 mm longitudinal pullback distance, corresponding to a 5,700 mm^2 area. The en face image shows gastric and esophageal mucosa separated by the GEJ (black dotted line). The capsule fiducial marks used for NURD correction appear as dark, longitudinal bands spanning the pullback (arrowheads). (B-D) Enlarged regions show a structured appearance of gastric mucosa compared to smooth esophageal mucosa. (E-F) Cross-sections of swine upper GI tract at two different longitudinal positions show structural differences between gastric and esophageal tissue. Fiducials appear as bright, hyper-scattering features (arrowheads) on the capsule window (arrow). Images are vertically cropped to remove the aliased inner surface of the capsule window. GEJ: gastroesophageal junction, Se: squamous epithelium, Lp: lamina propria, Mm: muscularis mucosa, Sm: submucosa

This is an important anatomical landmark, because Barrett's esophagus may originate or recur at the GEJ [49,50]. Enlarged insets show more detailed features, such as the textured appearance of gastric mucosa (Fig. 9(B), 9(C)) and the comparatively homogeneous appearance of esophageal mucosa (Fig. 9(D)). The cross sectional image of gastric mucosa shows gastric pit architecture, which generates vertical projection features, similar to columnar crypts in rectal mucosa (Fig. 9(E)). In the esophagus, the cross sectional image shows the layers of the mucosa and submucosa, including squamous epithelium, lamina propria, muscularis mucosa,

and submucosa (Fig. 9(F)). The rapid 30 mm/sec pullback speed and lubricious capsule design reduced non-uniform longitudinal motion distortion. Capsule contact to the mucosal wall was lost in a portion of the pullback. This was likely caused by the proximity to the gastric cardia, which balloons outward.

3.6. Widefield OCTA

The widefield OCTA probe was demonstrated for OCT angiographic imaging of the swine anorectal region (Fig. 10). The lower GI tract was imaged because it had less physiological motion and a shorter tether could be used, which enabled more uniform longitudinal actuation compared with the upper GI tract. OCTA was performed with a 600 Hz B-scan rate, corresponding to a ~1.6 ms interscan time, and a 760 mm^2 area was imaged in 7 seconds. Non-uniform longitudinal motion was minimized by the shallow insertion depth, and non-uniform rotational distortion was reduced using the 12 mm ball bearing motor.
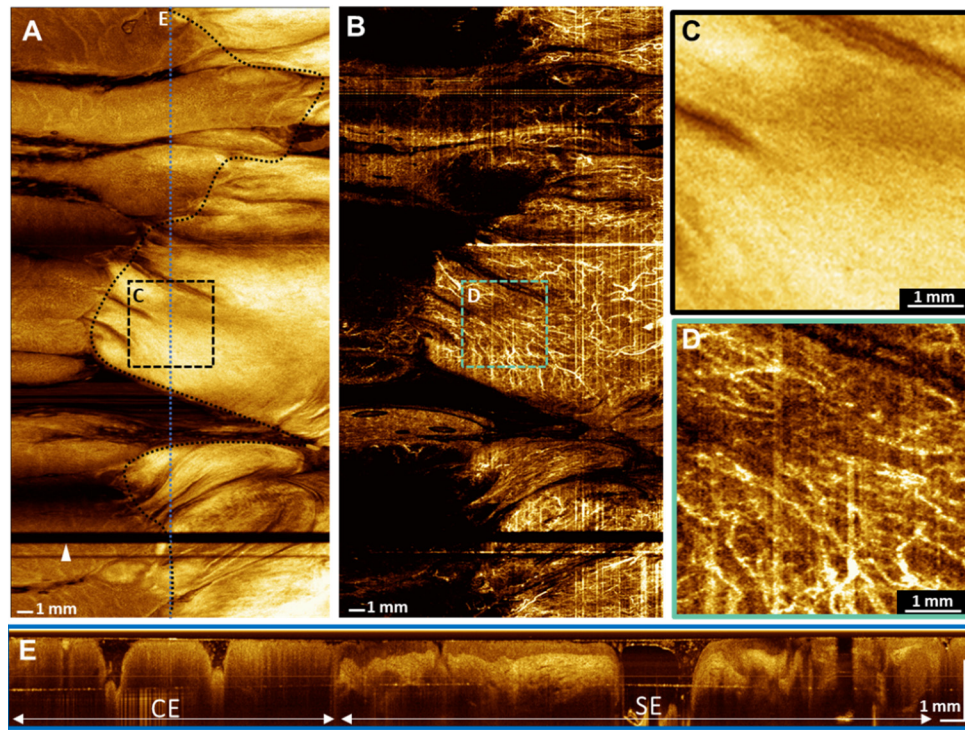

Fig. 10. (A) Widefield OCT en face image of the swine anorectal region, covering a 20 mm longitudinal pullback distance. The black-dotted line indicates the anorectal junction. The probe fiducial marker appears as a dark horizontal band (arrowhead). (B) En face OCTA image projected over the full axial depth. (C) Enlarged image of the squamous epithelium. (D) Enlarged image of the same region, showing anal canal microvasculature. (E) Cross sectional image spanning columnar epithelium and squamous epithelium. CE: columnar epithelium, SE: squamous epithelium.

Figure 10 shows OCT structural and angiographic images of the swine anorectal region. The structural en face image shows the anorectal junction, which appears as a boundary between the columnar epithelium of the rectum and squamous epithelium of the anal canal (Fig. 10(A)).

Columnar epithelial crypt features can be seen transitioning into smooth squamous epithelium at the anorectal junction, and non-uniform longitudinal pullback motion distortion is minimal.

Microvascular features can be seen spanning the rectum and anal canal in the en face image (Fig. 10(B)). Although vascular architecture cannot be seen in the enlarged structural image (Fig. 10(C)) of the anal canal, the corresponding OCTA image can visualize the microvascular network (Fig. 10(D)). Columnar epithelium can be seen transitioning into squamous epithelium in a cross sectional image spanning the anorectal junction (Fig. 10(E)).

4.　Discussion

This manuscript presents MEMS-VCSEL SS-OCT technology at multi-MHz rates. Sweep to sweep MZI calibration and resampling using dual channel acquisition enable high acquisition speeds and improved performance compared to optically clocked ADCs. Ultrahigh speed SS-OCT structural and OCTA imaging of the swine gastrointestinal tract was demonstrated using a suite of devices which have complementary capabilities and can be generalized to a range of medical imaging applications.

There were several additional considerations to optimize SS-OCT performance. First, we used fiber couplers instead of circulators in the interferometers to reduce polarization mode dispersion (PMD), which degraded the PSF. PMD in circulators arises from birefringent crystals and unequal optical path lengths traveled by orthogonal polarizations, causing a group delay difference. The design eliminated PMD but resulted in a 3-dB incident power reduction and a 3-dB collected signal reduction from the 50:50 coupler. However, this limitation was mitigated in part by using a high-power BOA, which enabled high output powers of 130 mW.

An additional advantage of the MEMS-VCSEL is the ability to switch operating modes and generate adjustable sweep rates. MZI sweep to sweep calibration was especially important for achieving high performance. Operating the MEMS at off-resonance sweep rates increases sweep to sweep frequency variation [44]. Furthermore, nonlinearity in the VCSEL frequency versus time sweep generates interference fringes with a wider bandwidth than with linear frequency sweeps. When OCT fringe frequencies approach the electronic detection bandwidth, the detection electronics nonlinear phase response can degrade the PSF. We demonstrated successful correction of frequency sweep variations and nonlinear phase response using MZI sweep to sweep calibration. Compensation parameters were determined by iteratively optimizing multiple PSF measurements spanning the imaging range [46]. These methods allow operation over a range of sweep rates, independent of the MEMS resonance constraints.

For applications requiring both high speed and long imaging range, frequency sweep linearization is desirable to efficiently use ADC bandwidth. However, linearization at multi-MHz speeds remains challenging due to the high quality factor of the MEMS resonance. Solutions requiring dynamic modeling of the MEMS, waveform shaping, or overdriving with sweep buffering may be needed to achieve linear sweeps at higher multi-MHz speeds. In order to achieve ultrahigh speeds, both the up and down frequency sweep from the MEMS-VCSEL are typically used (bidirectional sweeping). However, the up and down sweeps can have different frequency versus time behavior because the MEMS actuates under electrostatic force for the up sweep (long to short wavelength), but under spring force for the down sweep (short to long wavelength). Beam scanning can also produce asymmetries between the OCT signals from the up and down frequency sweeps. Although this effect was not present in the endoscopic studies described here, systems with galvanometer scanners can have a time dependent path length variation, generating a Doppler shift that affects the up and down frequency sweeps differently. Careful detector nonlinear phase compensation, phase registration, and optical alignment are needed to achieve submicron ranging accuracy.

Ultrahigh speed MEMS-VCSELs offer several advantages for high performance OCT applications. In gastroenterology, commercial endoscopic OCT systems such as volumetric laser endomicroscopy (VLE) were demonstrated to visualize subsurface features associated with dysplasia in patients with Barrett's esophagus [15]. However, the commercial OCT system

operates at 50 kHz A-scan rates and uses balloon probes, requiring acquisition times approaching 90 seconds [51]. MEMS-VCSEL SS-OCT at 600 kHz–1.2 MHz A-scan rates were previously demonstrated for gastrointestinal imaging, but speeds were limited because of optical ADC clocking [19,44,45]. FDMLs and stretched pulse frequency comb (SPFC) lasers have also been demonstrated for intravascular, retinal, and rat/mouse nerve imaging [4,20,33,52]. Although the speeds reported here are slower than the SPFC laser, the MEMS-VCSEL has the advantage of being adjustable, low cost, and manufacturable.

The micromotor OCT catheter demonstrated in this study can be applied to a wide range of medical imaging applications. It can be introduced through the working channel of endoscopes and other minimally invasive devices, and high resolution volumetric images of small regions can be acquired under visual guidance. Procedures such as biopsy, ablation, or surgery can be visualized by OCT in real time. The distal micromotor can achieve a 1500 Hz B-scan rate to provide dense longitudinal sampling and enable high resolution OCT/OCTA, while fast pullback speeds decrease acquisition times and reduce motion artifacts. Our B-scan rates were slower than heartbeat intravascular OCT, which used a 2.9 MHz A-scan rate multiplexed FDML source [4]; however, the catheter in heartbeat OCT had a ~2.6X smaller circumference and could be operated at faster scan rates without trading off sampling density.

Tethered OCT capsules can perform widefield volumetric mapping of luminal organs, such as the esophagus [48]. However, motion artifacts from non-uniform longitudinal motion or respiratory/cardiac motion can distort en face features and reduce image coverage [45]. We demonstrated capsule imaging at 3.0 MHz A-scan rate, 1100 Hz B-scan rate, and 30 mm/sec pullback speed to rapidly map a large longitudinal length of the upper GI tract. The ultrahigh A-scan rates achieved by the MEMS-VCSEL enable rapid tethered capsule pullback speeds which produce more uniform longitudinal actuation and reduce physiological motion distortion artifacts compared with slower speeds of 1 MHz A-scan rate and 300 Hz B-scan rates used in previous tethered capsule studies [18].

A prototype widefield OCTA probe was also demonstrated for imaging luminal organs. To the best of our knowledge, this is the first demonstration of a manually actuated probe for widefield OCTA imaging. Our group previously demonstrated a 5 cm circumference (16 mm diameter) balloon catheter for endoscopic OCTA at 1.2 MHz A-scan rate [19]. The micromotor and optics within the balloon catheter were proximally pulled back with a translation stage to generate OCTA volumes. In contrast, the faster A-scan rate of the current system generated comparable OCTA image quality using a manual pullback of a short probe. Furthermore, our probe had reduced pressure on tissue and improved visibility of smaller vessels, which tended to be compressed by the previous balloon probe.

OCT and OCTA image quality were limited by rotary (fast) scan and longitudinal pullback (slow) uniformity. NURD results in non-uniform scan periods, causing variation in the circumferential A-scan positions between consecutive B-scan images. NURD depends on the motor drive waveform, rotational inertia, bearing design, and lubrication. We found that a ball bearing motor had better rotational stability and generated higher quality OCTA images compared to brass sleeve or ring jewel bearing motors. Non-uniform longitudinal pullback causes stretching (too slow longitudinal motion) or compression (too rapid longitudinal motion) of en face features, which reduces coverage as well as hinders image interpretation. Non-uniform longitudinal motion also causes artifacts in OCTA. Longitudinal pullback produces an out-of-plane displacement of sequential B-scans, resulting in a bulk decorrelation in the entire B-scan image and a noise floor in the OCTA signal. If longitudinal pullback is too fast, the bulk OCTA decorrelation signal increases, limiting the ability to visualize small blood vessels. OCTA using a manual pullback can also have artifacts because the longitudinal pullback is not constant speed. The widefield OCTA probe performance could be improved by using a rigid rod for a more uniform

longitudinal pullback or by proximally pulling back the motor and optics within a transparent housing, rather than pulling back the entire probe in contact with tissue.

Although SS-OCT has performance advantages over spectral domain OCT (SD-OCT), widespread adoption is primarily limited by cost. MEMS-VCSELs can be manufactured at low cost using monolithic fabrication with wafer-scale production and testing. An electrically pumped 1050 nm MEMS-VCSEL (MEMS-eVCSEL) with >100 nm sweep range that does not require a pump laser, isolator, and wavelength division multiplexer has been recently demonstrated [53]. Electrical pumping technology further reduces cost and complexity and can be extended to 1310 nm MEMS-VCSELs.

5. Conclusions

We demonstrated MEMS-VCSEL SS-OCT technology and devices for multi-MHz endoscopic OCT and OCTA imaging in the swine GI tract at 2.4 MHz and 3.0 MHz A-scan rates. Dual channel acquisition enabled sweep to sweep wavenumber calibration for improved versatility and performance. The system achieved >100 dB sensitivities and 1.5-1.8 mm imaging ranges in air, with axial resolutions of 16.0 and 16.9 μm in air (~12.3 and ~13.0 μm in tissue) at 2.4 MHz and 3.0 MHz, respectively. We described a suite of imaging devices, including a micromotor OCT catheter for high resolution OCT/OCTA, a tethered OCT capsule for widefield volumetric mapping of luminal structures, and a widefield OCTA probe. The technology and operating parameters shown in this study can be extended to other applications, including endoscopic, laparoscopic, and minimally invasive imaging as well as non-destructive evaluation and testing.

References

1. D. Huang, E. A. Swanson, C. Lin, J. S. Schuman, W. G. Stinson, W. Chang, M. Hee, T. Flotte, K. Gregory, C. Puliafito, and J. G. Fujimoto, "Optical Coherence Tomography," Science. **20**, 1–26 (1991).
2. S. Yun, G. J. Tearney, J. de Boer, N. Iftimia, and B. E. Bouma, "High-speed optical frequency-domain imaging," Opt. Express **11**(22), 2953 (2003).
3. I. Grulkowski, J. J. Liu, B. Potsaid, V. Jayaraman, C. D. Lu, J. Jiang, A. E. Cable, J. S. Duker, and J. G. Fujimoto, "Retinal, anterior segment and full eye imaging using ultrahigh speed swept source OCT with vertical-cavity surface emitting lasers," Biomed. Opt. Express **3**(11), 2733 (2012).
4. T. Wang, T. Pfeiffer, E. Regar, W. Wieser, H. van Beusekom, C. T. Lancee, G. Springeling, I. Krabbendam, A. F. W. van der Steen, R. Huber, and G. van Soest, "Heartbeat OCT: in vivo intravascular megahertz-optical coherence tomography," Biomed. Opt. Express **6**(12), 5021 (2015).
5. R. F. Spaide, J. G. Fujimoto, N. K. Waheed, S. R. Sadda, and G. Staurenghi, "Optical coherence tomography angiography," Prog. Retinal Eye Res. **64**, 1–55 (2018).
6. O. O. Ahsen, Y. K. Tao, B. M. Potsaid, Y. Sheikine, J. Jiang, I. Grulkowski, T. H. Tsai, V. Jayaraman, M. F. Kraus, J. L. Connolly, J. Hornegger, A. Cable, and J. G. Fujimoto, "Swept source optical coherence microscopy using a 1310 nm VCSEL light source," Opt. Express **21**(15), 18021–18033 (2013).
7. T. H. Tsai, C. L. Leggett, and A. J. Trindade, "Optical coherence tomography in gastroenterology: a review and future outlook," J. Biomed. Opt. **22**(12), 1 (2017).
8. Y. Q. Xiong, Y. Mo, Y. Q. Wen, M. J. Cheng, S. T. Huo, X. J. Chen, and Q. Chen, "Optical coherence tomography for the diagnosis of malignant skin tumors: a meta-analysis," J. Biomed. Opt. **23**(02), 1 (2018).
9. C. Kut, K. L. Chaichana, J. Xi, S. M. Raza, X. Ye, E. R. McVeigh, F. J. Rodriguez, A. Quiñones-Hinojosa, and X. Li, "Detection of human brain cancer infiltration ex vivo and in vivo using quantitative optical coherence tomography," Sci. Transl. Med. **7**(292), 292ra100 (2015).

10. L. P. Hariri, D. C. Adams, J. C. Wain, M. Lanuti, A. Muniappan, A. Sharma, T. V. Colby, M. Mino-Kenudson, E. J. Mark, R. L. Kradin, H. Goulart, A. M. Tager, and M. J. Suter, "Endobronchial optical coherence tomography for low-risk microscopic assessment and diagnosis of idiopathic pulmonary fibrosis in vivo," Am. J. Respir. Crit. Care Med. **197**(7), 949–952 (2018).

11. J. Gallwas, L. Turk, H. Stepp, S. Mueller, R. Ochsenkuehn, K. Friese, and C. Dannecker, "Optical coherence tomography for the diagnosis of cervical intraepithelial neoplasia," Lasers Surg. Med. **43**(3), 206–212 (2011).

12. G. J. Tearney, M. E. Brezinski, B. E. Bouma, S. A. Boppart, C. Pitris, J. F. Southern, and J. G. Fujimoto, "In vivo endoscopic optical biopsy with optical coherence tomography," Science **276**(5321), 2037–2039 (1997).

13. A. F. Swager, A. J. de Groof, S. L. Meijer, B. L. Weusten, W. L. Curvers, and J. J. G. H. M. Bergman, "Feasibility of laser marking in Barrett's esophagus with volumetric laser endomicroscopy: first-in-man pilot study," Gastrointest. Endosc. **86**(3), 464–472 (2017).

14. S. J. Erickson-Bhatt, R. M. Nolan, N. D. Shemonski, S. G. Adie, J. Putney, D. Darga, D. T. McCormick, A. J. Cittadine, A. M. Zysk, M. Marjanovic, E. J. Chaney, G. L. Monroy, F. A. South, K. A. Cradock, Z. G. Liu, M. Sundaram, P. S. Ray, and S. A. Boppart, "Real-time imaging of the resection bed using a handheld probe to reduce incidence of microscopic positive margins in cancer surgery," Cancer Res. **75**(18), 3706–3712 (2015).

15. M. A. C. Rodriguez, D. T. H. de Moura, I. B. Ribeiro, W. M. Bernardo, F. H. A. Morita, S. B. Marques, P. Sakai, and E. G. H. de Moura, "Volumetric laser endomicroscopy and optical coherence tomography in Barrett's esophagus: a systematic review and meta-analysis," Endosc. Int. Open **07**(09), E1078–E1091 (2019).

16. M. R. Struyvenberg, A. J. De Groof, R. Fonollà, F. Van Der Sommen, P. H. N. De With, E. J. Schoon, B. L. A. M. Weusten, C. L. Leggett, A. Kahn, A. J. Trindade, E. K. Ganguly, V. J. A. Konda, C. J. Lightdale, D. K. Pleskow, A. Sethi, M. S. Smith, M. B. Wallace, H. C. Wolfsen, G. J. Tearney, S. L. Meijer, M. Vieth, R. Pouw, W. L. Curvers, and J. J. G. H. M. Bergman, "Prospective development and validation of a volumetric laser endomicroscopy computer algorithm for detection of Barrett's neoplasia," Gastrointest. Endosc. **93**, 871 (2020).

17. O. O. Ahsen, K. Liang, H. C. Lee, M. Giacomelli, Z. Wang, B. Potsaid, M. Figueiredo, Q. Huang, V. Jayaraman, J. G. Fujimoto, and H. Mashimo, "Assessment of Barrett's esophagus and dysplasia with ultrahigh-speed volumetric en face and cross-sectional optical coherence tomography," Endoscopy **51**, 355 (2018).

18. K. Liang, O. O. Ahsen, A. Murphy, J. Zhang, T. H. Nguyen, B. M. Potsaid, M. Figueiredo, Q. Huang, H. Mashimo, and J. G. Fujimoto, "Tethered capsule en face optical coherence tomography for imaging Barrett's esophagus in unsedated patients," BMJ Open Gastro **7**, e000444 (2020).

19. H. C. Lee, O. O. Ahsen, K. Liang, Z. Wang, C. Cleveland, L. Booth, B. Potsaid, V. Jayaraman, A. E. Cable, H. Mashimo, R. Langer, G. Traverso, and J. G. Fujimoto, "Circumferential optical coherence tomography angiography imaging of the swine esophagus using a micromotor balloon catheter," Biomed. Opt. Express **7**(8), 2927 (2016).

20. A. López-Marín, G. Springeling, R. Beurskens, H. van Beusekom, A. F. W. van der Steen, A. D. Koch, B. E. Bouma, R. Huber, G. van Soest, and T. Wang, "Motorized capsule for shadow-free OCT imaging and synchronous beam control," Opt. Lett. **44**(15), 3641 (2019).

21. T. Klein and R. Huber, "High-speed OCT light sources and systems [Invited]," Biomed. Opt. Express **8**(2), 828 (2017).

22. B. Braaf, K. A. Vermeer, V. A. D. P. Sicam, E. van Zeeburg, J. C. van Meurs, and J. F. de Boer, "Phase-stabilized optical frequency domain imaging at 1-μm for the measurement of blood flow in the human choroid," Opt. Express **19**(21), 20886 (2011).

23. R. Huber, "Fourier domain mode locking (FDML): A new laser operating regime and applications for biomedical imaging, profilometry, ranging and sensing," in *Optics InfoBase Conference Papers* (OSA, 2009), **14**(8), p. MA1.

24. R. Huber, D. C. Adler, and J. G. Fujimoto, "Buffered Fourier domain mode locking: unidirectional swept laser sources for optical coherence tomography imaging at 370,000 lines/s," Opt. Lett. **31**(20), 2975 (2006).

25. W. Wieser, B. R. Biedermann, T. Klein, C. M. Eigenwillig, and R. Huber, "Multi-Megahertz OCT: High quality 3D imaging at 20 million A-scans and 45 GVoxels per second," Opt. Express **18**(14), 14685 (2010).

26. T. Klein, W. Wieser, C. M. Eigenwillig, B. R. Biedermann, and R. Huber, "Megahertz OCT for ultrawide-field retinal imaging with a 1050 nm Fourier domain mode-locked laser," Opt. Express **19**(4), 3044 (2011).

27. S. Yamashita and M. Asano, "Wide and fast wavelength-tunable mode-locked fiber laser based on dispersion tuning," Opt. Express **14**(20), 9399 (2006).

28. Y. Takubo, T. Shirahata, and S. Yamashita, "Optimization of a dispersion-tuned wavelength-swept fiber laser for optical coherence tomography," Appl. Opt. **55**(27), 7749 (2016).

29. B. Johnson, W. Atia, D. C. Flanders, M. Kuznetsov, B. D. Goldberg, N. Kemp, and P. Whitney, "SNR of swept SLEDs and swept lasers for OCT," Opt. Express **24**(10), 11174 (2016).

30. X. Wei, J. Xu, Y. Xu, L. Yu, J. Xu, B. Li, A. K. S. Lau, X. Wang, C. Zhang, K. K. Tsia, and K. K. Y. Wong, "Breathing laser as an inertia-free swept source for high-quality ultrafast optical bioimaging," Opt. Lett. **39**(23), 6593 (2014).

31. J. Xu, X. Wei, L. Yu, C. Zhang, J. Xu, K. K. Y. Wong, and K. K. Tsia, "High-performance multi-megahertz optical coherence tomography based on amplified optical time-stretch," Biomed. Opt. Express **6**(4), 1340 (2015).

32. S. Tozburun, M. Siddiqui, and B. J. Vakoc, "A rapid, dispersion-based wavelength-stepped and wavelength-swept laser for optical coherence tomography," Opt. Express **22**(3), 3414 (2014).

33. M. Siddiqui, A. S. Nam, S. Tozburun, N. Lippok, C. Blatter, and B. J. Vakoc, "High-speed optical coherence tomography by circular interferometric ranging," Nat. Photonics **12**(2), 111–116 (2018).

34. D. Huang, F. Li, Z. He, Z. Cheng, S. Chao, and P. K. Wai, "400 MHz ultrafast optical coherence tomography," Opt. Lett. **45**(24), 6675–6678 (2020).
35. N. Lippok, B. E. Bouma, and B. J. Vakoc, "Highly-stable, multi-megahertz circular-ranging optical coherence tomography at 1.3 um," Biomed. Opt. Express **11**(1), 174 (2020).
36. T. S. Kim, J. Joo, I. Shin, P. Shin, W. J. Kang, B. J. Vakoc, and W.-Y. Oh, "9.4 MHz A-line rate optical coherence tomography at 1300 nm using a wavelength-swept laser based on stretched-pulse active mode-locking," Sci. Rep. **10**(1), 9328 (2020).
37. V. Jayaraman, G. D. Cole, M. Robertson, A. Uddin, and A. Cable, "High-sweep-rate 1310 nm MEMS-VCSEL with 150 nm continuous tuning range," Electron. Lett. **48**(14), 867 (2012).
38. OptoRes, "NG-FDML | Multi-MHz Swept Laser," 1–2 (n.d.).
39. C. Jirauschek and R. Huber, "Wavelength shifting of intra-cavity photons: Adiabatic wavelength tuning in rapidly wavelength-swept lasers," Biomed. Opt. Express **6**(7), 2448 (2015).
40. K. C. Liang, Z. Wang, O. O. Ahsen, H. C. Lee, B. M. Potsaid, V. Jayaraman, A. Cable, H. Mashimo, X. D. Li, and J. G. Fujimoto, "Cycloid scanning for wide field optical coherence tomography endomicroscopy and angiography in vivo," Optica **5**(1), 36–43 (2018).
41. O. O. Ahsen, H. C. Lee, M. G. Giacomelli, Z. Wang, K. Liang, T. H. Tsai, B. Potsaid, H. Mashimo, and J. G. Fujimoto, "Correction of rotational distortion for catheter-based en face OCT and OCT angiography," Opt. Lett. **39**(20), 5973–5976 (2014).
42. J. P. Gordon and H. Kogelnik, "PMD fundamentals: Polarization mode dispersion in optical fibers," Proc. Natl. Acad. Sci. U. S. A. **97**(9), 4541–4550 (2000).
43. A. H. Dhalla, K. Shia, and J. A. Izatt, "Efficient sweep buffering in swept source optical coherence tomography using a fast optical switch," Biomed. Opt. Express **3**(12), 3054 (2012).
44. T. H. Tsai, H. C. Lee, O. O. Ahsen, K. Liang, M. G. Giacomelli, B. M. Potsaid, Y. K. Tao, V. Jayaraman, M. Figueiredo, Q. Huang, A. E. Cable, J. G. Fujimoto, and H. Mashimo, "Ultrahigh speed endoscopic optical coherence tomography for gastroenterology," Biomed. Opt. Express **5**(12), 4387 (2014).
45. K. Liang, G. Traverso, H. C. Lee, O. O. Ahsen, Z. Wang, B. Potsaid, M. Giacomelli, V. Jayaraman, R. Barman, A. Cable, H. Mashimo, R. Langer, and J. G. Fujimoto, "Ultrahigh speed en face OCT capsule for endoscopic imaging," Biomed. Opt. Express **6**(4), 1146 (2015).
46. Z. Wang, B. Potsaid, L. Chen, C. Doerr, H. C. Lee, T. Nielson, V. Jayaraman, A. E. Cable, E. A. Swanson, and J. G. Fujimoto, "Cubic meter volume optical coherence tomography," Optica **3**(12), 1496 (2016).
47. A. Zhang, Q. Zhang, C. L. Chen, and R. K. Wang, "Methods and algorithms for optical coherence tomography-based angiography: a review and comparison," J. Biomed. Opt. **20**(10), 100901 (2015).
48. K. Liang, O. O. Ahsen, H. C. Lee, Z. Wang, B. M. Potsaid, M. Figueiredo, V. Jayaraman, A. E. Cable, Q. Huang, H. Mashimo, and J. G. Fujimoto, "Volumetric mapping of Barrett's esophagus and dysplasia with en face optical coherence tomography tethered capsule," Am. J. Gastroenterol. **111**(11), 1664–1666 (2016).
49. J. Que, K. S. Garman, R. F. Souza, and S. J. Spechler, "Pathogenesis and cells of origin of Barrett's esophagus," Gastroenterology **157**(2), 349–364.e1 (2019).
50. S. S. Sami, A. Ravindran, A. Kahn, D. Snyder, J. Santiago, J. Ortiz-Fernandez-Sordo, W. K. Tan, R. A. Dierkhising, J. E. Crook, M. G. Heckman, M. L. Johnson, K. Lansing, K. Ragunath, M. Di Pietro, H. Wolfsen, F. Ramirez, D. Fleischer, K. K. Wang, C. L. Leggett, D. A. Katzka, and P. G. Iyer, "Timeline and location of recurrence following successful ablation in Barrett's oesophagus: An international multicentre study," Gut **68**(8), 1379–1385 (2019).
51. C. L. Leggett, E. C. Gorospe, D. K. Chan, P. Muppa, V. Owens, T. C. Smyrk, M. Anderson, L. S. Lutzke, G. J. Tearney, and K. K. Wang, "Comparative diagnostic performance of volumetric laser endomicroscopy and confocal laser endomicroscopy in the detection of dysplasia associated with Barrett's esophagus," Gastrointest. Endosc. **83**(5), 880–888.e2 (2016).
52. S. Chang, E. Murdock, Y. Mao, C. Flueraru, and J. Disano, "Stationary-fiber rotary probe with unobstructed 360° view for optical coherence tomography," Opt. Lett. **36**(22), 4392 (2011).
53. V. Jayaraman, C. Burgner, J. Carter, I. Borova, N. Bramham, C. Lindblad, and A. Cazabat, "Widely tunable electrically pumped 1050 nm MEMS-VCSELs for optical coherence tomography," in *Vertical-Cavity Surface-Emitting Lasers XXIV*, C. Lei and L. A. Graham, eds. (SPIE, 2020), (May), p. 27.